nature communications

Article

https://doi.org/10.1038/s41467-025-67784-4

Near-surface liquid water on Mars inferred from seasonal marsquakes

Received: 24 April 2025

Accepted: 9 December 2025

Jing Shi[1], Jiaqi Li[1,2,3], Caoanla Li[4,5], Haoran Meng[6], Cong Sun[6], Chao Qi[7], Lu Pan[8], Siteng Fan[6], Zhenliang Tian[6], Tao Wang[9], Lian Xue[1], Xie Hu[10] & Ling Chen[11]

Exploring the presence and behavior of water on Mars is critical for understanding the planet's geological evolution, hydrological processes, and potential habitability, which has been a central objective of past and ongoing Martian exploration missions. Martian geomorphology provides evidence of ancient groundwater activity, but confirmation of present-day liquid water remains limited. Here, we infer near-surface brines confined to meter-scale depths in regions north of about 30 °N in the northern hemisphere, based on the analysis of seasonal variations in marsquake seismicity and thermal modeling. The absence of seasonal marsquakes during colder periods and their abrupt resurgence in warmer seasons can be explained by ice-to-brine phase transitions. Our findings reveal a mechanism whereby seasonal melting of subsurface ice elevates pore pressure and lubricates faults, leading to a reduction in frictional strength, and ultimately inducing marsquakes. This mechanism accounts for the seasonal variation, clustering, high seismic *b*-values, and shallow focal depths of seasonal marsquakes. Additionally, we estimate that the melting point of briny ice on Mars is below approximately 250 ± 13 K, advancing our understanding of Mars' present-day brine cycle and near-surface hydrological processes.

The presence of subsurface (meter-scale) liquid brines on present-day Mars is crucial for assessing the planet's habitability, evolution, and the possibility of the existence of living or ever-lived organisms[1,2]. Water ice is widespread on Mars from the polar regions[3,4], down to the subsurface of mid-latitudes[5,6]. The widespread ground ice distribution is supported by water ice exposed at recent craters and retreating scarps[7,8], glacial landforms with viscous flow features[9,10], dielectric properties consistent with water ice from radar images[11,12], as well as the hydrogen-rich deposits poleward of latitudes ±60 ° identified from the Mars Odyssey Neutron Spectrometer[13,14]. Although current Mars surface conditions are not favorable for liquid water to persist, concentrated saline solutions, or liquid brines, are predicted to be stable under Martian conditions in theory[15,16].

Recent discoveries of seasonal varying features on Mars (e.g., recurring slope lineae)[17,18] suggest possibly indirect evidence of liquid brines that transiently flow on the Martian surface[19], while their morphology does not allow the exclusion of the alternative possibility of granular flows[20]. Other geomorphological evidence, including gullies, slope streaks, and flow-like features in the polar regions, that might support the existence of liquid brines in the subsurface, also has alternative dry interpretations[21]. Radar data reveal strong reflectors at the base of Mars' south polar cap that suggest the potential presence of a subglacial lake beneath the south pole[22], but the typical local geothermal heat flux does not allow for the basal melting of polar ice caps[23,24]. Thermodynamic calculations suggest that groundwater may exist in Mars' subsurface today, while it likely resides at kilometer-scale depths beyond the detection limits of orbital radar[25]. Thus, merely based on remote sensing observations, the existence and potential distribution of liquid brines in the subsurface of Mars remains ambiguous.

A full list of affiliations appears at the end of the paper. e-mail: JLI@pku.edu.cn

The physical properties of subsurface materials can provide inferences about the presence of liquid brines. Electrically, the presence of liquids increases the dielectric permittivity of the medium, detectable by orbital or in-situ radar on Mars[22,26]. Seismically, subsurface liquids alter the elastic and anelastic properties of the underground mass, which can be analyzed through detecting changes in seismic wave speeds and attenuation[27]. Analysis of crustal velocities derived from marsquake data recorded by the SEIS (Seismic Experiment for Interior Structure) seismometer aboard the InSight (Interior Exploration using Seismic Investigations, Geodesy, and Heat Transport) lander[28] reveals that the Martian upper crust, approximately 10 km thick below the landing site at Elysium Planitia (Fig. 1a), lacks a thick (i.e., kilometer-scale) cryosphere[29]. Beneath this region, the mid-crust (~10–20 km deep) is hypothesized to potentially host water or other volatiles based on the interpretation of seismic velocities with lithology models[30]. Conversely, coda wave analysis of marsquakes suggests that the crust traversed by the seismic waves may contain minimal amounts of volatiles and is predominantly dry[31,32].

Variations in seismic activity can serve as a valuable proxy for detecting liquids in regions beyond the landing site of ground-penetrating radar or seismometer. On Earth, natural processes such as groundwater recharge from snowmelt during warm seasons often lead to increased seismicity in volcanic[33,34] and glacial[35] regions. In addition, artificial fluid injection into the subsurface, such as during industrial activities, also triggers seismic events, a phenomenon known as "induced seismicity"[36]. That is, an increase in seismicity may indicate groundwater recharge.

Seasonal variations of marsquake seismicity have been observed on Mars. In the marsquake catalogue compiled by the InSight Marsquake Service (MQS)[37,38], tectonic marsquakes, classified as low-frequency and broadband events, are relatively well understood in terms of their both mechanism and location[37,38], with their occurrence showing no significant temporal variation. In contrast, another group of marsquakes, often referred to as the 2.4-Hz and high-frequency events[39,40], exhibits clear seasonal variations in occurrence rate (hereafter termed seasonal marsquakes). However, the driving mechanism behind seasonal marsquakes remains unclear[37].

The seismicity of seasonal marsquakes predominantly occurs between solar longitudes Ls = 33 and Ls = 187[40]. Seasonal marsquakes were initially identified through seismicity analyses conducted during the first Martian year of the InSight mission (corresponding to MY35: Martian Year 35)[40], and were subsequently corroborated using an expanded dataset from the second Martian year (corresponding to MY36: Martian Year 36)[41,42]. Previous studies have identified seasonal marsquakes as a response to variations in illumination conditions, rather than tidal forces and the carbon dioxide cycle[40]. Nevertheless, the fundamental question of how illumination modulates this seismic activity remains unknown.

In this study, we investigated the mechanism underlying the seismicity of seasonal marsquakes. Our analysis focused on the abrupt onset of seasonal marsquakes around early spring (Ls = 25) in the northern hemisphere and the decline in their occurrence rate near the summer-fall transition (Ls = 200). We also examined the spatial clustering characteristics and the Gutenberg-Richter seismic b-value[43] of seasonal marsquakes. Based on these observations, we proposed that the seismic activity of seasonal marsquakes indicates the presence of briny ice and its phase transition to brines, initiating in the meter-scale subsurface and extending to greater depths on present-day Mars.

Results and discussion

Rapid change in occurrence rates of seasonal marsquakes

We focused on the seismic activity of seasonal marsquakes occurring during the early nighttime hours, specifically from local mean solar time (LMST) 17:00 to 24:00, the quietest period of a day at the InSight landing site on Mars (Fig. 2a). During the daytime, the strong wind noise dominates the recordings of the InSight SEIS seismometer, making the detection of seasonal marsquakes challenging (Fig. 2a).

We hypothesized that the seasonal marsquakes observed at night represent continuous processes initiated during the daytime, when illumination and temperature changes likely exert stronger control on

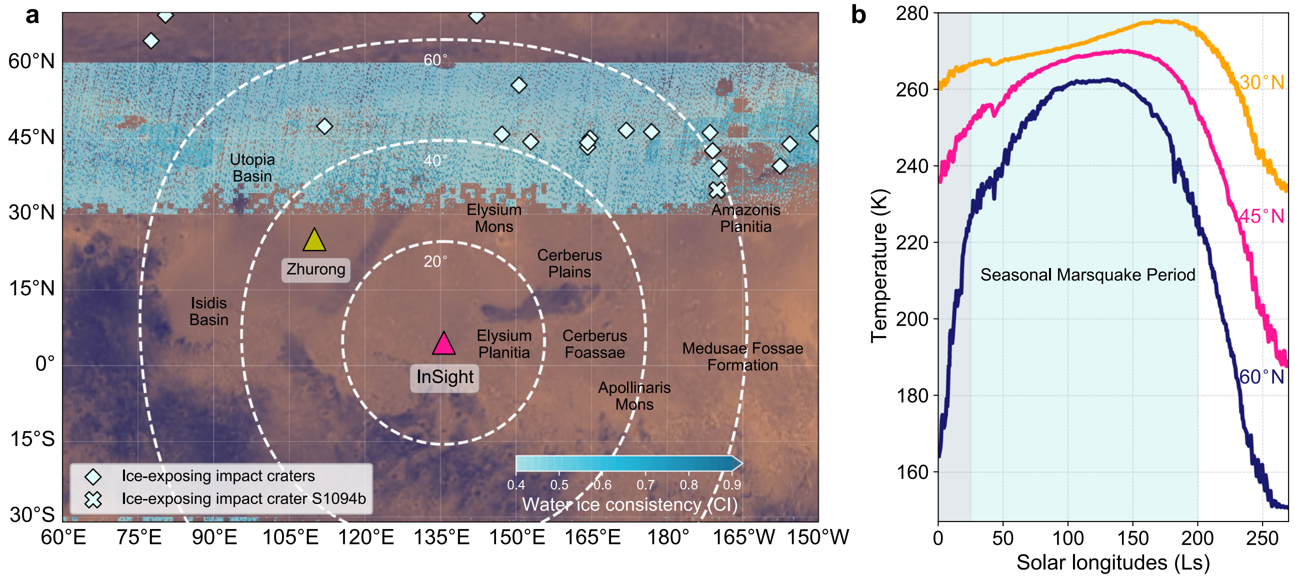

Fig. 1 | Location of InSight and seasonal variations of average midday surface temperature. **a** Location of InSight on Mars (red triangle). The base map is a colorized mosaic of Viking orbiter images. The mid-latitude band (30°N–60°N) shows the water-ice consistency (within 1–5 m depth) from ref. 73. White diamonds indicate craters excavating subsurface ice[98]; the white cross denotes the S1094b impact site (recorded by InSight) that exposed ice-rich materials[74]. The yellow triangle marks the landing site of Zhurong. White dashed curves depict regions centered on InSight with epicentral distances of 20°, 40°, and 60°. **b** Seasonal variation of average midday surface temperature in Martian Year 35 for the northern mid-latitudes. Yellow, red, and dark blue curves represent temperature variations at 30°N, 45°N, and 60°N (80°E to 180°E longitude range), respectively. The gray transparent box indicates the period without seasonal marsquakes, and the blue transparent box marks the period associated with seasonal marsquake activity.

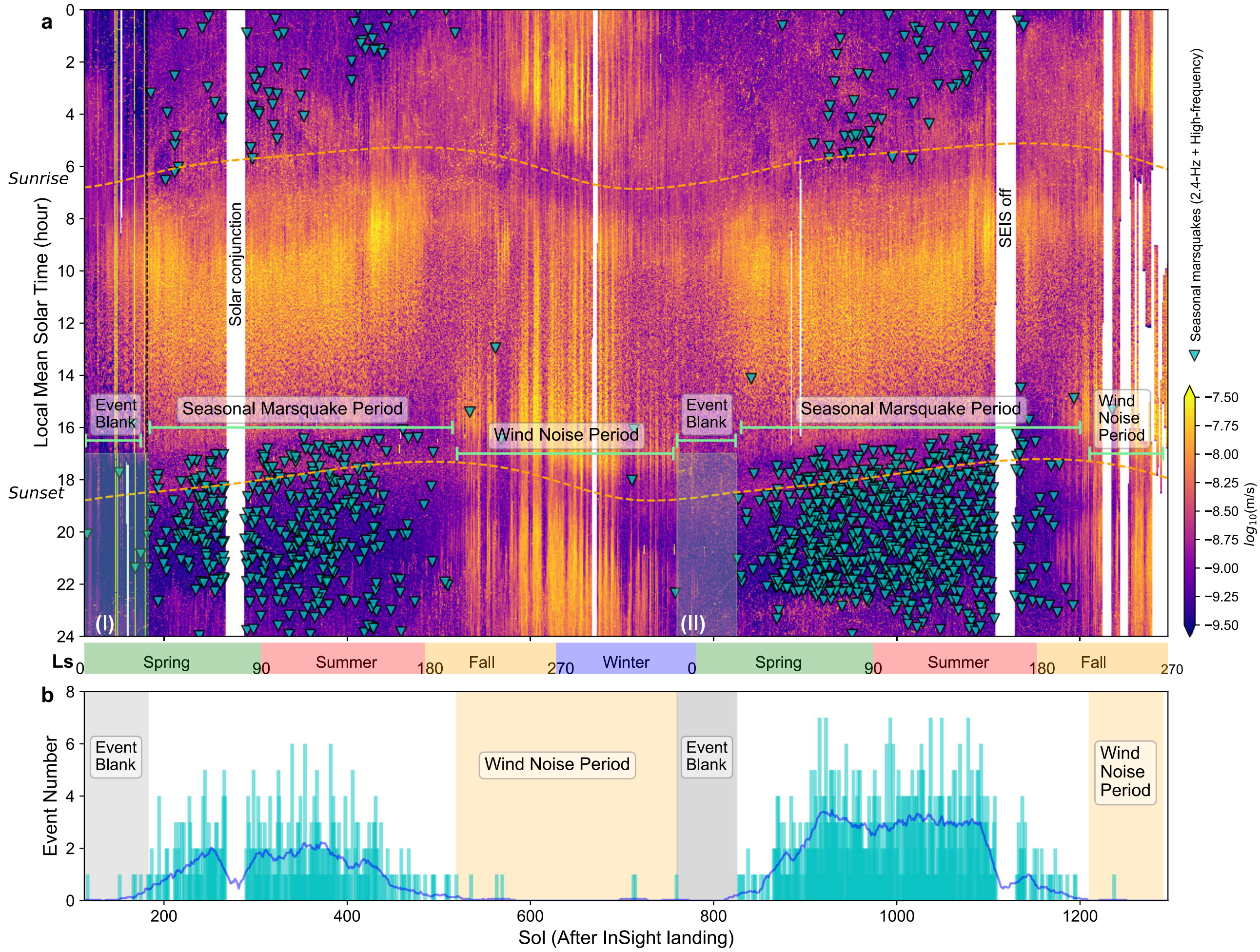

Fig. 2 | Seismicity analysis of seasonal marsquakes. a Mean seismic background noise levels, quantified by the root mean square (RMS) of seismic amplitudes recorded on the vertical component of InSight's seismometer. Overlaid are the origin times of seasonal marsquakes (cyan triangles). Amplitude data are band-pass filtered to 0.02–8.0 Hz and log-scaled for clarity; higher RMS values indicate greater background noise levels. Data before sol 182 (black dashed vertical line) are obtained from the short-period seismometer, and subsequent data are from very broadband seismometer[28]. The *y*-axis represents local mean solar time, with two orange dashed curves indicating the sunrise and sunset. The *x*-axis (shared with **b**) represents solar days (sols, one Martian year is approximately 688 sols) after InSight's landing. The corresponding solar longitudes (Ls) and Martian northern-hemisphere seasons are indicated between panels. Green horizontal markers partition the marsquake catalogue into three distinct periods: a period of event blank (highlighted by gray transparent boxes, I and II), with low background noise but very few seasonal marsquakes; a period dominated by seasonal marsquakes; and a period with strong wind noise during fall and winter. White areas indicate data gaps, including the solar conjunction and the seismometer (SEIS) off. **b** Daily occurrence counts of seasonal marsquakes (cyan bars). The solid blue line represents the moving average of the daily occurrence rate of seasonal marsquakes. Periods of event blank and wind noise (from **a**) are marked by gray and orange transparent boxes, respectively.

seismic activity. In contrast, nighttime temperatures on Mars remain consistently and extremely low throughout the year, regardless of the season[44], reducing the potential influence of illumination- or temperature-driven variations on seismic activity during this period.

The occurrence rate of seasonal marsquakes can be used to evaluate the potential presence of subsurface liquid brines. If seasonal temperature fluctuations were the sole driving factor, the seismicity rate would likely follow a gradual trend, reflecting the continuous nature of temperature changes. In contrast, the presence of subsurface liquid brines involves phase transitions between ice and brines, which would result in abrupt changes in seismic activities[33–35,45].

Seasonal marsquakes are virtually absent in the northern early spring (Ls = 0 to Ls = 25), according to the official marsquake catalogue[40,46]. This absence cannot be explained by unfavorable noise conditions. Noise levels during this period (gray transparent boxes I and II in Fig. 2a) are comparable to, or even lower than, those observed during the spring-summer transition, when the seismicity of seasonal marsquakes reaches its peak (Supplementary Fig. 1). This contrast highlights that the paucity of seasonal marsquakes in early spring is a distinct phenomenon, emerging under optimal detection conditions. To evaluate potential catalogue incompleteness, we applied template-matching analysis across a range of detection thresholds (Supplementary Text S1). The results confirm that no substantial number of detectable seasonal marsquakes was missed.

The observation is consistent across both the full dataset (Fig. 2) and the high-quality dataset, which includes only events above the completeness magnitude threshold (Supplementary Figs. 2 and 3). In contrast, tectonic marsquakes are more evenly distributed across spring and summer (Supplementary Fig. 4) and occur at a low and steady rate of approximately 0.1 events per Martian day (Supplementary Fig. 5). Additionally, we ruled out the possibility that tidal forces, one of the drivers of seismic activity on the Moon[42,47], play any significant role in modulating seasonal marsquakes on Mars, as no clear time correlation between them has been observed and insufficient tide-induced stress to trigger seasonal marsquakes (Supplementary Text S2). We also excluded carbon dioxide sublimation as the primary mechanism triggering

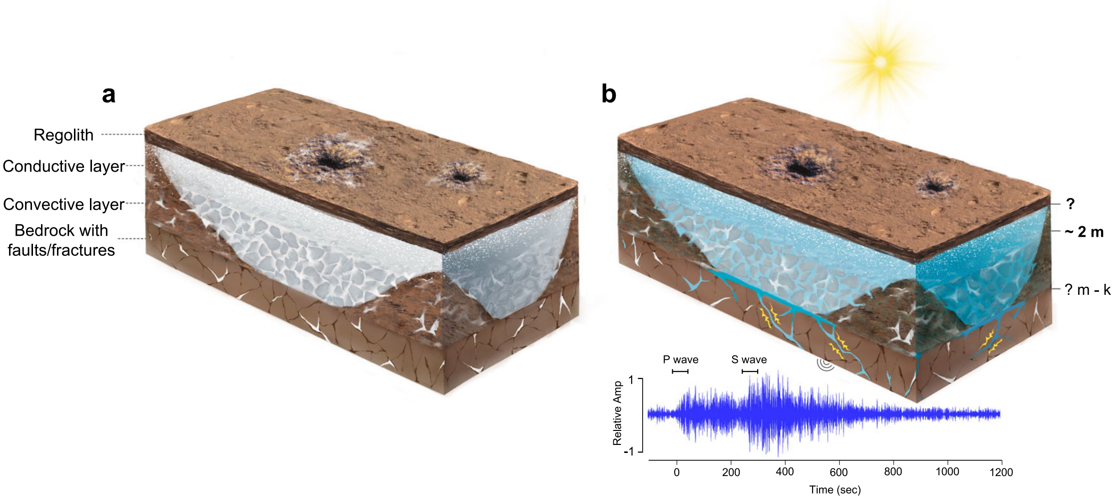

Fig. 3 | Schematic diagram of seasonal groundwater-induced marsquakes. **a** During the cold season, subsurface ice cements pore spaces, sealing faults and fractures. **b** During the warm season, briny ice melts in the conductive layer (top ~2 meters) with increasing temperatures. The resulting brines migrate downward, driven by gravity as well as salinity gradients, penetrating into the convective layer, facilitating further ice melting, and ultimately reaching deep-seated faults within the bedrock. The associated reduction in effective normal stress and the friction coefficient promotes fault slip and triggers marsquakes. The white dots show salinity distribution: salts concentrate in the near surface and decrease with depth, forming a vertical salinity gradient. The blue trace shows a representative waveform of a seasonal marsquake (event S0331a) recorded on the vertical component of the InSight's seismometer. The x-axis represents time relative to the direct P wave, and the y-axis shows relative amplitude. The two horizontal lines with short bars mark the arrival times of the direct P wave and S wave, respectively. Note that sizes in the schematic view are not necessarily to scale.

seasonal marsquakes because its annual pressure variations (below 250 Pa)[48] are orders of magnitude smaller than the thousands of pascals typically required to induce seismic activity[49,50].

Surface warming fuels seasonal marsquakes

The abrupt changes in the seismicity of seasonal marsquakes (Fig. 2) suggest that the events are likely triggered with a threshold limit. Although seasonal marsquakes in the northern hemisphere coincide with warmer periods, their abrupt onset cannot be explained by temperature or illumination alone. If either factor were the sole driver force, the occurrence rate would vary gradually, mirroring the smooth seasonal evolution of these parameters. While diurnal temperature variations can trigger thermal marsquakes (i.e., super-high-frequency events)[51], these are small in magnitude, last only a few tens of seconds, and are confined to the vicinity of the InSight lander[41,51]. In contrast, seasonal marsquakes are larger in magnitude up to Mw ~3.0[37], last for hundreds of seconds (Fig. 3b), and occur at epicentral distances beyond 20° (~1200 km)[39,41,52].

Furthermore, seasonal marsquakes can be detected at night, indicating that illumination alone is unlikely to sustain this seismic pattern. Illumination-driven effects, such as thermal expansion and contraction, are transient by nature and dissipate quickly after sunset, corresponding to the occurrence of thermal marsquakes[41,44,51]. In contrast, if groundwater processes are the driver, the movement of liquid brines would facilitate gradual subsurface pressure redistribution and sustained fault instability, extending seismic activity beyond the window of direct solar heating.

To explain the rapid and distinct variations in seasonal marsquakes, we proposed a model where the melting of ice triggers these events (Fig. 3). During cold seasons (Fig. 3a), pore spaces are ice-cemented, resulting in relatively stronger faults that are less prone to slip. In warm seasons (Fig. 3b), however, the melting of ice into brine elevates pore pressures and lubricates faults[53,54], a process that reduces the effective normal stress and friction coefficient, thereby promoting slip and inducing marsquakes. In this model, surface warming drives seismic activity by promoting the phase transitions from ice to brine. Consequently, higher temperatures lead to the increased melt production, thereby promoting seismicity. This mechanism explains why the peak occurrence of seasonal marsquakes aligns with the warm season in the northern hemisphere.

By analogy, seasonal marsquakes would also be expected in the southern hemisphere warm season (i.e., northern fall and winter) if substantial subsurface ice exists in the southern hemisphere. However, the seismic catalogue reveals virtually no events during this period[40,46], owing to high wind-generated noise (Fig. 2a), which severely impedes detection even with template-matching approaches. Crucially, this observational gap does not weaken our model, as the conclusive evidence comes from the low-noise windows of the northern early spring (gray transparent boxes I and II in Fig. 2a). The near-absence of marsquakes in early spring, followed by a sharp surge at the spring-summer transition, robustly supports a phenomenon concentrated in the northern hemisphere and driven by temperature-dependent ice melting (Fig. 3). The application of novel detection techniques to the existing dataset, as well as future missions targeting the southern hemisphere or operating under quieter conditions, will provide critical opportunities to test and refine our model.

Marsquake clustering linked to localized brines activity

The spatial clustering of seasonal marsquakes reinforces the hypothesis of subsurface brines on Mars. If temperature or illumination were the sole drivers of seasonal marsquakes, their effects would likely influence a broad spatial region, resulting in a diffuse distribution of events. However, the observed clustering of seasonal marsquakes is inconsistent with a solely temperature- or illumination-driven mechanism.

Two key observations underscore the spatial clustering of seasonal marsquakes. First, these events are clustered in terms of epicentral distance. For most seasonal marsquakes, the arrival time differences between the direct P and S waves are consistently around 249 ± 24 s (Supplementary Fig. 6 and refs. 39,41,55). Second, the scattering and attenuation properties of the medium along the propagation paths of seasonal marsquakes also exhibit clustering. The P- and S-wave rise times, which reflect the medium scattering properties[56,57], are concentrated around 80 ± 16 s and 106 ± 18 s, respectively (Supplementary

Fig. 7a, b). Additionally, the consistency in quality factors of coda waves (3300 ± 980) further confirms the clustering (Supplementary Fig. 7c).

For outliers in the clusters and a few events occurring within the event gap shown in Fig. 2a, they may arise from the classification methodology employed in the official marsquake catalogue[37,38]. Notably, all marsquakes analyzed in this study are categorized as either 2.4-Hz events or high-frequency events in the catalogue. While these two categories generally exhibit seasonal variation and clustering, they should not be strictly equated with seasonal marsquakes. The current classification method relies on seismogram spectra rather than underlying mechanisms, which may result in events from different processes (e.g., meteorite impact) being grouped together. Nonetheless, these outliers do not affect our hypothesis of brine-related processes, as most events show clear seasonal variation, clustering, and high occurrence rates.

High seismic *b*-value for seasonal marsquakes

A high seismic *b*-value (2.81) has been observed for seasonal marsquakes[58]. However, the underlying cause of this observation is unexplored. Here, we suggested that the elevated *b*-value may serve as another independent indicator of subsurface liquid brines.

The seismic *b*-value, as defined in the Gutenberg-Richter law[43], characterizes the magnitude-frequency relationship of seismic events, with higher *b*-values indicating a greater proportion of smaller magnitude events. Terrestrial observations and laboratory experiments have shown that the seismic *b*-value is inversely related to the differential stress[59–61]. The presence of fluids can increase pore pressures, thereby reducing effective normal stress. This reduction in effective normal stress facilitates fault slip at lower differential stresses, resulting in higher *b*-values[62].

For tectonic marsquakes, which exhibit no seasonal variation, the seismic *b*-value is approximately 1.31 ± 0.18 (see "Methods," and also refs. 58,63), similar to that of tectonic earthquakes on Earth[60]. In contrast, the *b*-value for seasonal marsquakes is significantly higher, even considering uncertainties (2.42 ± 0.10 in this study; see "Methods"; 2.81 in ref. 58). This notably elevated seismic *b*-value for seasonal marsquakes provides additional evidence for the presence of liquids on Mars, consistent with observations from terrestrial analogs such as magma chambers in volcanic regions[64], fluid-injection wells[62], and snowmelt zones[65].

Shallow brine reservoir and melting dynamics

The temperature dependence of seasonal marsquakes constrains the depth range of subsurface liquid brines to the conductive zone influenced by temperature. To estimate this depth, we modeled the subsurface annual temperature profile using the heat conduction equation. The input surface temperature was derived from the Mars Climate Database[66], where we extracted the daily maximum surface temperature curve (Supplementary Fig. 8a) over a Martian year at the InSight landing site. Thermal diffusivity of the subsurface material may carry significant uncertainties; thus, we adopted two distinct values of thermal diffusivity: $5.1 \times 10^{-8}\ \mathrm{m^2\,s^{-1}}$ for the Martian soil measured at the InSight[44,67], and $7 \times 10^{-7}\ \mathrm{m^2\,s^{-1}}$ for buried rocks[44,68].

Our calculation indicates that the thermally affected depth ranges from approximately 1.3 to 3.5 m (Supplementary Fig. 8b, c), consistent with previous estimates[44]. While this result is specific to the InSight landing site, similar depths would be expected in regions with comparable thermal properties. The meter-scale thickness of this conductive zone suggests that seasonal temperature variations are limited to shallow depths (~2.0 m). If present, any ice within this narrow layer could therefore sustain liquid brines during periods when temperatures rise above the eutectic point.

Notably, although the bottom of the conductive layer (Fig. 3a) lies at about 2.0 m depth, the total amount of melted liquid is not confined to this shallow zone. This depth marks the boundary for heat conduction (Fig. 4a), yet salinity-driven convection (Fig. 4b) can transport heat and salts downward, enabling the melting of deeper ice. Here, convection denotes the compositional process arising from brine-ice interactions, initiated by salinity gradients, rather than bulk fluid circulation. More specifically, during warm seasons, surface heating raises the temperature within the shallow conductive layer above the eutectic point of water and common salts (e.g., perchlorates, chlorates, and sulfates)[69], producing a partially molten mixture of ice and brine (Fig. 3b). The brines, which are denser than ice, gas, and low-salinity water, migrate downward under gravity through pore spaces. Driven by salinity gradients, this meltwater sinks, pushing the brine front deeper than would be allowed by heat conduction alone. As melting proceeds, the latent heat consumed gradually cools the brine, which keeps thermally driven melting relatively shallow. In turn, salinity-driven convection becomes the dominant force driving ice melting at greater depths.

To test whether salinity-driven convection can melt the underlying ice under isothermal conditions with brine and ice at the same temperature, we performed controlled laboratory experiments (see Methods). The results consistently show that once formed, the brine readily melts the ice underneath (Supplementary Fig. 9 and Fig. 4c and Supplementary Movies 1–5), as the melting point of ice is depressed by dissolved salts. While variables like temperature, acrylic content (analogous to Martian rock fragments), and salt concentration affect the percolation rate and depth, melting still occurs. Besides, the salinity-driven convection is also confirmed by recent experimental, theoretical, and numerical studies on permafrost thawing[70].

Having established the viability of ice melting, a key requirement for our conceptual model of Mars (Fig. 3) is to explain how brines can penetrate to depths of hundreds or thousands of meters to reach the bedrock with faults. The experiment (Supplementary Movie 1) reveals a mechanism capable of enabling this rapid and deep percolation: channelization. We observed that the development of channels during percolation (Fig. 4c–e) enhances downward flow rates by up to orders of magnitude. On Earth, injection-induced earthquakes demonstrate that fluid conduits facilitate rapid transport, greatly reducing the time for fluids to reach seismogenic faults and induce slip[71]. On Mars, comparable pathways such as fractures and other heterogeneities may serve as natural conduits. Therefore, the channelization observed in our experiments offers a compelling mechanism for how brines exploit these subsurface features to achieve the necessary penetration depths.

Our experiments confirm that brine percolation is viable under isothermal conditions. Although conducted at the centimeter scale, the governing physical factors, such as permeability, brine supply, and fracture connectivity, are scale-independent, implying that the qualitative behavior may extend to Martian environments. Quantitative extrapolation to relevant field scales, however, must account for coupled nonlinear dynamics across meter to hectometer depths. These dynamics include interactions among temperature evolution, freeze-thaw cycles, heterogeneous ice saturation, and evolving permeability. Critically, certain Martian conditions, such as seasonal thermal gradients, freeze-front propagation rates, capillary forces, and reduced gravity, cannot be fully reproduced in laboratory experiments. While these factors limit precise quantitative projection, they do not diminish the fundamental physical plausibility of brine infiltration on Mars.

The infiltration depth, probably extending to hundreds of meters to a few kilometers, aligns with the shallow crustal origin inferred for seasonal marsquakes[39]. For example, waveform comparisons show that seasonal marsquakes resemble impact events (focal depth: 0 km) more closely than tectonic marsquakes (focal depth > 10 km) (e.g., Supplementary Fig. 10). This similarity supports a shallow origin of seasonal marsquakes. Additionally, the depth range matches the slip or rupture lengths estimated from the seismic magnitudes (Mw 1.2–3.0)

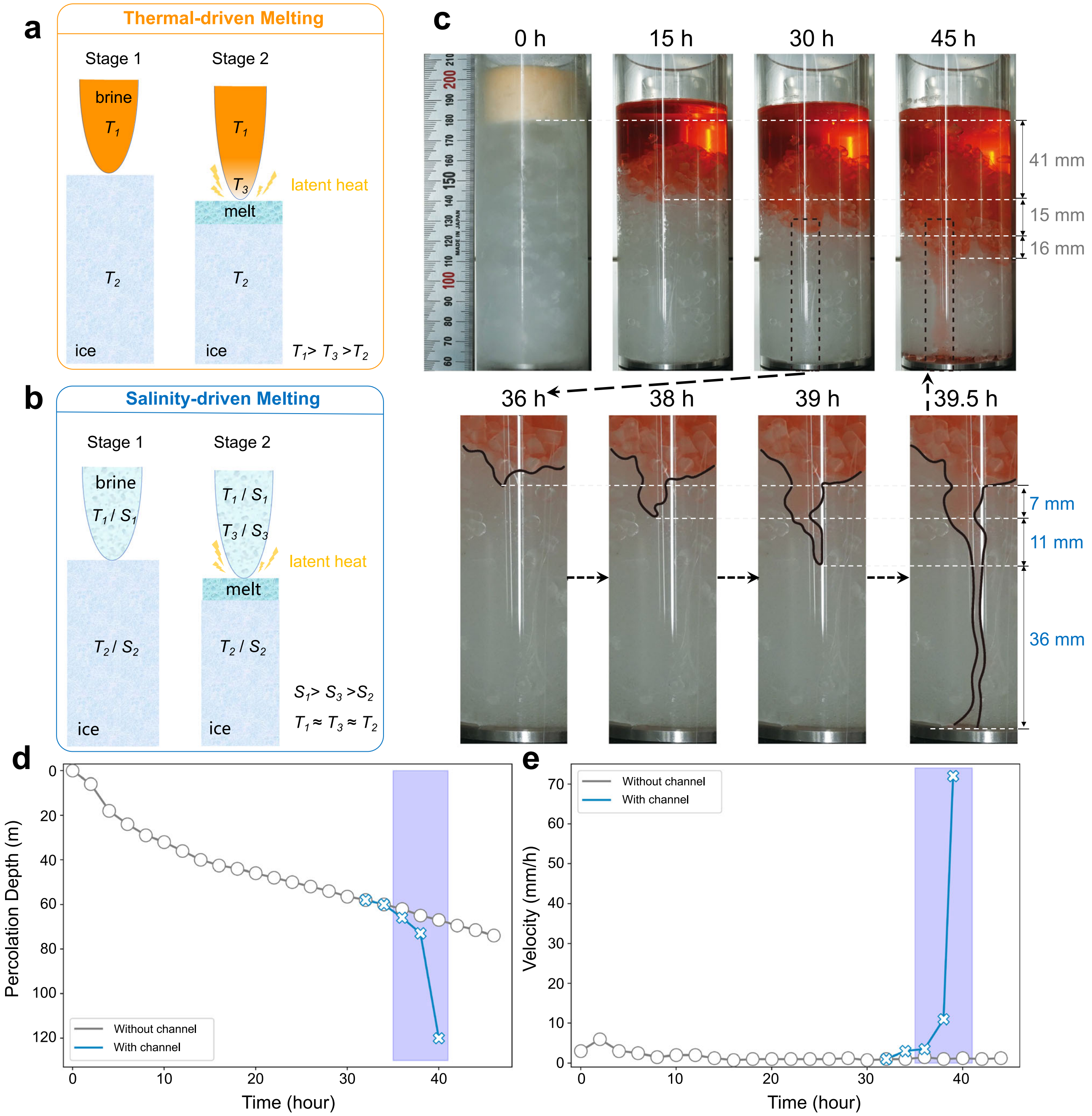

Fig. 4 | Laboratory simulation of salinity-driven convection in brine-ice systems. a Conceptual diagram of thermal-driven melting. In this case, melting is controlled by the temperature gradient, where the brine temperature (T_1) exceeds the interface temperature (T_3), and T_3 exceeds the ice temperature (T_2). **b** Conceptual diagram of salinity-driven melting. The addition of salt lowers the melting point of ice, enabling melting even without a temperature gradient. Critically, a vertical salinity gradient is required: brine salinity (S_1) is higher than the salinity at the brine-ice interface (S_3), and S_3 exceeds the salinity within the ice (S_2). **c** Time-lapse snapshots of brine percolation in laboratory simulations of salinity-driven convection. Experimental conditions: −5 °C, 11 vol.% acrylic beads, and 15 wt.% NaCl brine (see "Methods" for details). The brine and the underlying ice are maintained at the same temperature to replicate conditions in the convective layer below the conductive zone. The black box highlights a close-up view after channel formation. Black dashed arrows indicate the time sequence, and white horizontal lines mark the percolation front at various stages. Supplementary Movie 1 shows the complete experimental process. Cumulative percolation depths at corresponding times are noted on the right. **d** Temporal evolution of percolation depth over time. The *x*-axis shows experimental time, and the *y*-axis denotes percolation depth. Blue crosses and gray circles correspond to depths in channelized and non-channelized regions, respectively. The blue transparent box highlights the increased percolation depth and rate in the channelized region. **e** Percolation velocity as a function of time.

of seasonal marsquakes[37,38]. The rupture sizes range from 47 to 373 m in ice, 31 to 249 m in frozen soil, and 22 to 173 m in crustal rock (see Methods).

The shallow heat conduction boundary rules out the possibility that seasonal marsquakes are triggered by the freezing of aquifers and the associated volumetric expansion during colder seasons (in the southern hemisphere), a mechanism proposed prior to the landing of the InSight mission[72]. This is because, unlike the warming mechanism, where both conduction and convection processes are involved, the cooling mechanism relies solely on heat conduction, which affects only shallow depths on the meter scale. As a result, an approximately 10% volumetric expansion within the top few meters, associated with the brine-to-ice phase transition, is likely insufficient to generate seasonal marsquakes with seismic magnitudes ranging from Mw 1.2 to 3.0[37,38]. However, while we excluded freezing and volume expansion as mechanisms for the seasonal marsquakes recorded by the InSight, we did not rule out the possibility of such events occurring in regions beyond the sensitivity of the InSight seismometer. Future seismological missions can help validate this freezing and volume expansion mechanism.

Where to find near-surface brines

The location of the brine reservoir responsible for seasonal marsquakes must meet two key requirements. First, daily midday temperatures at this location need to rise continuously after Ls = 25, corresponding to the onset of seasonal marsquakes in the northern early spring (Fig. 2a). Second, these elevated temperatures need to persist long enough (e.g., from Ls = 25 to Ls = 200) to sustain conditions favorable for seasonal marsquakes (Fig. 2b).

Regions north of about 30 °N satisfy both requirements and emerge as the most plausible source for near-surface brines (Fig. 1b and Supplementary Fig. 11c). In contrast, low-latitude regions either exhibit a temperature decrease after Ls = 25 (Supplementary Fig. 11a) or show a significantly delayed temperature peak (Supplementary Fig. 11b). The inferred brine source locations are consistent with previous studies, including the water-ice consistency map[73], which indicates subsurface ice at depths of 1–5 m across the mid-latitudes (30 °N–60 °N) (Fig. 1a). At the same time, observations of bright material excavated from impact craters north of 30°N[8,74] (Fig. 1a) have been interpreted as exposures of shallow ice. Moreover, in-situ measurements by Zhurong identified hydrated minerals and dust, suggesting recent groundwater rising or melting of subsurface ice at its landing site, which is located near the mid-latitudes of Utopia Planitia[75] (Fig. 1a).

The brine reservoirs, however, are likely spatially localized rather than widespread for two main reasons. First, the narrow range of arrival time differences between P and S waves for seasonal marsquakes indicates similar epicentral distances[39,41,55]. Second, the large quality factor (~2500–6900) measured from the coda waves of seasonal marsquakes (Supplementary Fig. 12) suggests that the Martian crust along the propagation paths from the source to the InSight is generally very dry[31]. This measurement rules out the widespread underground water but consistent with localized reservoirs in the source region.

Taken together, these observations support the hypothesis that the brine source for seasonal marsquakes is localized and situated in the north of about 30 °N. Regions with subsurface brine may have the potential to preserve organic materials and microbial life, offering critical insights into Mars habitability. Both the American Mars Sample Return mission and China's Tianwen-3 mission are equipped with drilling systems capable of reaching depths of approximately 2–3 m[76,77], which aligns with the range of near-surface brines inferred from this study. Consequently, these regions represent highly promising candidates for landing sites in the context of the Mars Sample Return mission.

Melting point of subsurface ice

Seasonal marsquakes emerge after Ls = 25 (Fig. 2), at which point the surface temperature, according to the proposed model (Fig. 3), provides an upper bound on the melting point of subsurface ice. The midday (LMST 10:00–14:00) surface temperature at the onset (Ls = 25) of seasonal marsquakes within the potential brine source regions (Fig. 1b) is approximately 250 ± 13 K, as derived from the Mars Planetary Climate Model (see "Methods"). A melting point of at least 23 K lower than that of pure ice (273 K) strongly suggests the presence of brines. While temperature alone cannot fully determine brine composition, a melting point below 250 ± 13 K provides a critical and independent constraint. Such constraints may be combined with other approaches, such as the seismo-electric method of ref. 78, to further characterize aquifers within the Martian crust.

Water volume required to induce seasonal marsquakes

Laboratory and field studies on Earth demonstrate that relatively small pore pressure perturbations (~0.01–0.1 MPa) can trigger earthquakes when faults are near failure[49,79]. Thus, seasonal marsquakes are likely to exhibit comparable sensitivity under near-failure conditions. Such pore pressure perturbations can be achieved during fluid injection[49,79], for example, in wastewater disposal operations, where fluid is injected at moderate pressures, distinct from high-pressure hydraulic fracturing, into deep geological formations. Critically, the process of injecting wastewater into deep aquifers on Earth is analogous to our model where meltwater percolates to deeper faults on Mars. Well-documented researches of wastewater disposal on Earth has quantified a systematic positive correlation between the volume of injected fluid and the maximum induced seismic magnitude[80]. Thus, by projecting the observed magnitudes of seasonal marsquakes onto this Earth-derived relationship (Supplementary Fig. 13), we estimated that a fluid volume of ~0.1 m^3 per unit area (equivalent to 0.1 m water depth) would be sufficient to trigger seasonal marsquakes with maximum moment magnitudes (Mw) of ~3.0.

The estimate of the required water volume assumes that fault slip is primarily driven by elevated pore pressure. Meanwhile, our proposed model incorporates another complementary process: the same brines responsible for melting may also reduce the effective friction coefficient along fault planes. This dual mechanism (pore-pressure enhancement and friction reduction) would act synergistically to lower the threshold for fault activation. Consequently, if both processes operate in tandem, the meltwater volume required to trigger seasonal marsquakes could be even smaller.

To assess whether the estimated water volume could be generated under Martian conditions with latent heat included, we performed thermal conduction modeling. Our synthetic calculations show that, given a melting point of 240 K, seasonal surface temperature variations can bring the melting isotherm to a depth of ~2 m within the conductive layer under a porosity of 0.4 (Supplementary Fig. 14). This penetration depth yields a meltwater volume per unit area of ~0.7 $m^3 m^{-2}$ (Supplementary Text S3) that exceeds the threshold of 0.1 $m^3 m^{-2}$ required to induce marsquakes. Below this conductive layer, salinity-drive melting in the underlaying convective zone generates substantially more fluids, further supporting the physical mechanism proposed for induced seasonal marsquakes.

Annual variations in seismicity?

In addition to seasonal variation, annual temperature changes may also regulate ice-brine phase transitions, potentially driving yearly fluctuations in the occurrence rate of seasonal marsquakes. The total number of seasonal marsquakes detected between MY35 and MY36 exhibits a distinct annual variation, with the number recorded in MY36 nearly doubling that of MY35 (734 versus 417) (Fig. 2b). This trend holds true even when considering only events above the completeness magnitude (Supplementary Figs. 2 and 15), with MY36 still showing approximately 100 more seasonal marsquakes than MY35. In contrast, the number of tectonic marsquakes remains relatively stable between the two years (46 in MY35 versus 49 in MY36).

We investigated whether the increased seismic activity of seasonal marsquakes in MY36 is associated with annual temperature variations. Using Mars Planetary Climate Model (see "Methods"), we compared the average midday (LMST 10:00–14:00) surface temperatures between MY36 and MY35 during Ls = 25 to Ls = 200, the period when seasonal marsquakes occur (Fig. 2). Since nighttime temperatures on Mars are consistently low[44] and do not affect brine-ice transitions, midday period is more relevant for this analysis.

Based on the proposed surface warming hypothesis (Fig. 3), seasonal marsquakes are concentrated in the northern hemisphere. The Mars Planetary Climate Model reveals that in several mid-latitude regions, including the north of the Utopia Planitia, mean surface temperatures during warm seasons (Ls = 25 to Ls = 200) in MY36 are higher than in MY35, with a maximum difference exceeding 4.0 K (Supplementary Figs. 16 and 17). This increase in temperature may have contributed to enhanced amount of molten brines, potentially driving the higher occurrence of seasonal marsquakes in MY36.

However, caution is needed when interpreting the correlation between the occurrence rates of seasonal marsquake and annual temperature variations. First, the two-year marsquake catalogue may not provide a statistically reliable basis for annual analysis. Second, the largest recorded quake, S1222a (Mw 4.7 ± 0.2)[81], occurred near the end of MY36, suggesting that stress state may have been higher in MY36 than in MY35. This could influence the occurrence of seasonal marsquakes with moderate magnitudes (Mw 1.2–3.0), though it likely did not affect larger tectonic marsquakes.

Near-surface brines cycle on Mars

To sustain the seasonal variation of seismicity, both the inflow and outflow of brines are essential. Without inflow at shallow depths, brine reservoirs on Mars would gradually deplete, preventing the occurrence of seasonal marsquakes. Similarly, without outflow at greater depths, brines could remain stagnant, potentially triggering seismic events year-round.

Water inflow may originate from Mars' interior through non-eruptive degassing in volcanic regions[82] or other processes. Numerical simulations suggest that present-day water in Martian interior can be released into the atmosphere via non-eruptive degassing processes and subsequently accumulate as ice in the shallow subsurface or on the surface[82]. Over time, a layer of dust can protect these ice deposits, likely allowing them to build up to several meters in thickness. This accumulation could provide a sufficient ice reservoir that, when melted, would reinfiltrate into the subsurface, completing a hydrological cycle on Mars. Alternatively, modern atmospheric water, in the form of frost or snow on Mars, may also contribute to the water inflow[83].

Sustaining the brine circulation also requires a continuous salt supply to maintain the necessary chemical gradients. Multiple processes likely contribute to the enrichment of salts in the shallow subsurface, such as the deposition of dust-borne salts (e.g., perchlorates, sulfates, and chlorides)[84]. Additionally, relict evaporitic deposits from past aqueous activity, along with ongoing atmospheric-surface interactions, may serve as further supplementary sources[85].

Brine outflow could occur through crustal faults. Shallow groundwater infiltrates deep regions, triggering seismic fault slip and rupture. This fault movement creates new pathways within the Martian crust, facilitating the downward migration of brines into deeper layers, a process commonly observed on Earth[86]. Therefore, seasonal marsquakes resulting from repeated cycles of stress redistribution and fluid infiltration can, in turn, activate previously isolated hydrological processes along seismic faults.

Methods

Calculation of the seismic *b*-value

We calculated the *b*-value using two different methods: least squares regression and maximum likelihood estimation[87,88]. The two methods, respectively, present seismic *b*-values of 2.52 and 2.42 for seasonal marsquakes, with an average of 2.47 (Supplementary Fig. 18a), and the maximum likelihood estimation gives one standard deviation of 0.10. This is in sharp contrast to the lower *b*-value (least squares regression: 1.07, maximum likelihood estimation: 1.31 ± 0.18) for tectonic marsquakes (Supplementary Fig. 18b), findings that align closely with prior research[58]. In addition, a remarkable increase in the *b*-value of seasonal marsquakes is observed from MY35 to MY36, rising from 2.2 to 2.9 (Supplementary Fig. 18c). This increase may reflect the influence of surface temperature changes, where warming enhances the phase transition from ice to brine, thereby contributing to the higher number of small seasonal marsquakes observed in MY36 compared to MY35.

Laboratory experiments for salinity-driven convection

To illustrate the potential of the salinity-driven convection model in triggering seasonal marsquakes, we conducted a series of laboratory experiments on the infiltration of brine through ice-acrylic mixtures. By maintaining isothermal conditions between brine and ice, these experiments were designed to replicate brine percolation within the convective layer, where temperature variations are minimal.

In this framework, the ice-acrylic mixtures serve as analogues for Martian frozen soil in the convective layer, while the overlying brine represents meltwater derived from an ice-rich shallow surface. By systematically varying experimental temperature, acrylic content (to simulate the fraction of soil or rock fragments), and NaCl brine salinity, we investigated how these parameters influence brine percolation. This approach enabled us to evaluate the applicability of the salinity-driven convection model to plausible Martian settings.

Sample preparation followed a standard ice synthesis method[89]. Ice cubes made from ultrapure water were crushed at −25 to −35 °C, sieved at −20 to −25 °C, and sorted into particle sizes of 180–250 μm. Cylindrical acrylic particles (~3 mm in diameter, 5–7 mm in height) were then mixed uniformly with the sieved ice powder, packed into a transparent cylindrical acrylic mold (~5 cm in diameter), and sealed with metal plugs fitted with O-rings. An aluminum spacer with small holes was inserted above the mixture to allow fluid exchange during evacuation. Because acrylic has low thermal conductivity, the assembly was equilibrated for one hour in an environmental chamber as the temperature increased from −30 to −3 °C. The mold was then connected to a vacuum line, air was removed while immersed in an ice-water bath, and degassed ultrapure water was introduced into the pores of the mixture. Freezing was induced from the bottom by placing the mold on a copper plate inside a freezer (−35 to −30 °C) and insulating it with a polyester foam sleeve. After overnight freezing, the mold contained the intact ice-acrylic sample, ready for experiments.

Brines were prepared by dissolving 15 or 20 wt.% NaCl in ultrapure water, with food coloring added to trace infiltration pathways. Prior to each run, frozen brine was crushed into powders and compacted onto the sample surface at −30 °C. The samples were then transferred to an environmental chamber maintained at −5 or −10 °C. Supplementary Table 1 summarizes the experimental conditions, including chamber temperature, acrylic content, and brine salinity. Throughout each experiment, a Sony ILCE-7M4 camera captured time-lapse images at one-minute intervals, and demonstration videos were later compiled.

The experiments consistently demonstrate that salinity-driven convection enhances the ability of brine to melt underlying ice (Supplementary Fig. 9). All runs were maintained for more than 45 h, ensuring that the percolation velocity stabilized. Results show that brine infiltration reliably induces melting of the underlying ice, with percolation depths varying according to experimental conditions. In addition, compositional convection is observed during the later stage of each experiment: salt enrichment promotes melting at greater depths, while re-precipitation of ice occurs in shallower layers.

Among the parameters tested, temperature exerts the strongest control. An increase of 5 °C in chamber temperature results in nearly a fourfold increase in percolation depth (Supplementary Fig. 9b, e). Acrylic content also plays a significant role, with up to a 3.5-fold increase in percolation depth between mixtures containing 0 and 55 vol.% acrylic (Supplementary Fig. 9c, d). The presence of acrylic, serving as a rock analogue, promotes melting along phase boundaries in the two-phase ice-rock system, though the difference between 21 and

55 vol.% acrylic is modest. By comparison, brine salinity exerts only a moderate influence: an increase of 5 wt.% in NaCl concentration produces a smaller enhancement (~1.3 times) in percolation depth (Supplementary Fig. 9a, b) than either temperature or acrylic content.

Most critically, once channelization occurs during percolation, both infiltration depth and rate increase by nearly an order of magnitude (Fig. 4). This nonlinear transition highlights the fundamental role of preferential flow paths in accelerating brine transport. Complete experimental videos illustrating these processes are provided in the Supplementary Materials.

Rupture size estimation for Mw 1.2–3.0 marsquakes

According to Hanks and Kanamori[90], the relationship between seismic moment M_0 and moment magnitude M_w is given by:

$$M_w = (\log_{10} M_0 - 9.05)/1.5, \tag{1}$$

where M_0 is measured in $\mathrm{N \cdot m}$. Seasonal marsquakes with M_w from 1.2 to 3.0 then correspond to seismic moments of $7.08 \times 10^{10}\,\mathrm{N \cdot m}$ to $3.55 \times 10^{13}\,\mathrm{N \cdot m}$. For seismic events with $M_w \le 6$ that do not saturate the seismogenic zone, a circular crack model is commonly assumed. The scalar seismic moment of such events can be estimated by:

$$M_0 = \left(\frac{16}{7}\right)\mu \Delta\varepsilon R^3, \tag{2}$$

where R is the radius, μ is the shear modulus, and $\Delta\varepsilon$ is the uniform strain drop, typically assumed to be 10^{-4} [91]. Adopting strain drops of 10^{-3} or 10^{-5} would not significantly affect the estimated magnitude but would lead to approximately a factor of 2.15 variation in the inferred rupture radius.

On Mars, the surface rocks are predominantly tholeiitic basalts, formed through extensive partial melting and exhibiting minimal weathering. These rocks typically have a shear modulus of 20–40 GPa[92]. In comparison, the shear modulus of freshwater ice and briny ice is approximately 3 GPa[93], while frozen soil exhibits temperature-dependent variations in shear modulus, generally ranging from 6 to 15 GPa. For the purpose of this analysis, representative shear modulus values of 3, 10, and 30 GPa are adopted for ice, frozen soil, and Martian crustal rock, respectively.

Using these shear moduli, the estimated rupture radius for seasonal marsquakes with $M_w \sim 1.2$ to 3.0 range from 47 to 373 m in ice, 31–249 m in frozen soil, 22–173 m in crustal rock. The corresponding rupture areas, determined using:

$$A = \pi R^2, \tag{3}$$

are approximately 6.9×10^3 to $4.4 \times 10^5\,\mathrm{m}^2$ for ice, 3.0×10^3 to $1.9 \times 10^5\,\mathrm{m}^2$ for frozen soil, 1.5×10^3 to $9.4 \times 10^4\,\mathrm{m}^2$ for crustal rock (Supplementary Table 2).

Calculation of the average midday surface temperatures

The surface temperatures of Mars were obtained from the widely used Mars Planetary Climate Model (Mars PCM), developed at the Dynamic Meteorology Laboratory (LMD), which is extensively utilized within the planetary science community. Mars PCM is a general circulation model, which consists of a dynamical core that uses a finite difference method to solve primitive equations and a physical core considering a series of comprehensive processes, such as radiative transfer[94], the dust cycle[95], the water cycle, and energy and material transfer in the planetary boundary layer (PBL) region.

The temperature variations of Mars, including seasonal and interannual changes, are closely linked to the distribution characteristics of Martian dust. The vertical distribution of dust particles in the Mars PCM is derived using a semi-interactive method. In this study, we employed daily column-integrated dust scenarios based on comprehensive reconstruction dust maps, which provide the 9.3 μm absorption column dust optical depth for multiple Martian years (from MY24 to MY36). These maps are described in detail by Montabone et al.[96]. By using these semi-interactive dust scenarios and the corresponding input data, we were able to achieve atmospheric and surface temperatures that closely align with actual observations.

In addition, the surface temperature of the Martian is influenced by surface thermodynamic processes dominated by thermal inertia and surface-soil thermal conduction, as well as phase transition processes of surface CO_2 and water, and boundary layer mixing. On a diurnal timescale, it is also affected by the local topography, including slope and shadow effects. In the simulations we conducted, all of these physical processes were enabled to ensure that the Mars PCM simulation results closely resemble actual conditions.

The horizontal resolution of the simulations is 5.625 × 3.75 degrees with 73 sigma-pressure levels covering the altitude range from near surface to ~250 km. We conducted multiple Mars PCM simulations for different Martian years (MY30 to MY36) using the corresponding reconstruction dust maps and interpolated the surface temperature data from the simulation results to local mean solar time (LMST). Subsequently, we applied average kernel processing to the data near midday (LMST 10:00–14:00), obtaining surface temperature values for different Martian sols around local noon.

Data availability

The processed data generated in this study are available at the Zenodo repository (https://zenodo.org/records/17765768). Data obtained from other sources are cited with the corresponding references. We utilized the Marsquake catalogue compiled by the InSight Marsquake Service (MQS)[37], which provides key information for each event, including origin time, type, and quality.

Code availability

All the code to reproduce the figures is available in the Zenodo repository[97]: https://zenodo.org/records/17765768.

References

1. Michalski, J. R. et al. Groundwater activity on Mars and implications for a deep biosphere. *Nat. Geosci.* **6**, 133–138 (2013).
2. Hurowitz, J. A. et al. Redox-driven mineral and organic associations in Jezero Crater, Mars. *Nature* **645**, 332–340 (2025).
3. Ojha, L., Nerozzi, S. & Lewis, K. Compositional constraints on the north polar cap of Mars from gravity and topography. *Geophys. Res. Lett.* **46**, 8671–8679 (2019).
4. Titus, T. N., Kieffer, H. H. & Christensen, P. R. Exposed water ice discovered near the South Pole of Mars. *Science* **299**, 1048–1051 (2003).
5. Piqueux, S. et al. Widespread shallow water ice on Mars at high latitudes and mid latitudes. *Geophys. Res. Lett.* **46**, 14290–14298 (2019).
6. Putzig, N. E. et al. Ice resource mapping on Mars. in *Handbook of Space Resources* 583–616 (Springer International Publishing, 2023).
7. Byrne, S. et al. Distribution of mid-latitude ground ice on Mars from new impact craters. *Science* **325**, 1674–1676 (2009).
8. Dundas, C. M. et al. Widespread exposures of extensive clean shallow ice in the midlatitudes of Mars. *JGR Planets* **126**, e2020JE006617 (2021).
9. Head, J. W., Marchant, D. R., Dickson, J. L., Kress, A. M. & Baker, D. M. Northern mid-latitude glaciation in the Late Amazonian period of Mars: criteria for the recognition of debris-covered glacier and valley glacier landsystem deposits. *Earth Planet. Sci. Lett.* **294**, 306–320 (2010).

10. Hubbard, B., Souness, C. & Brough, S. Glacier-like forms on Mars. *Cryosphere* **8**, 2047–2061 (2014).
11. Plaut, J. J. et al. Radar evidence for ice in lobate debris aprons in the mid-northern latitudes of Mars. *Geophys. Res. Lett.* **36**, 2008GL036379 (2009).
12. Mouginot, J. et al. The 3–5MHz global reflectivity map of Mars by MARSIS/Mars Express: implications for the current inventory of subsurface H2O. *Icarus* **210**, 612–625 (2010).
13. Feldman, W. C. et al. Global distribution of near-surface hydrogen on Mars. *J. Geophys. Res.* **109**, 2003JE002160 (2004).
14. Boynton, W. V. et al. Distribution of hydrogen in the near-surface of Mars: evidence for subsurface ice deposits. *Science* **297**, 81–85 (2002).
15. Brass, G. W. Stability of brines on Mars. *Icarus* **42**, 20–28 (1980).
16. Martínez, G. M. & Renno, N. O. Water and brines on Mars: current evidence and implications for MSL. *Space Sci. Rev.* **175**, 29–51 (2013).
17. McEwen, A. S. et al. Seasonal flows on warm martian slopes. *Science* **333**, 740–743 (2011).
18. McEwen, A. S. et al. Recurring slope lineae in equatorial regions of Mars. *Nat. Geosci.* **7**, 53–58 (2014).
19. Ojha, L. et al. Spectral evidence for hydrated salts in recurring slope lineae on Mars. *Nat. Geosci.* **8**, 829–832 (2015).
20. Dundas, C. M. et al. Granular flows at recurring slope lineae on Mars indicate a limited role for liquid water. *Nat. Geosci.* **10**, 903–907 (2017).
21. Bhardwaj, A., Sam, L., Martín-Torres, F. J. & Zorzano, M. Are slope streaks indicative of global-scale aqueous processes on contemporary Mars? *Rev. Geophys.* **57**, 48–77 (2019).
22. Orosei, R. et al. Radar evidence of subglacial liquid water on Mars. *Science* **361**, 490–493 (2018).
23. Sori, M. M. & Bramson, A. M. Water on Mars, with a grain of salt: local heat anomalies are required for basal melting of ice at the south pole today. *Geophys. Res. Lett.* **46**, 1222–1231 (2019).
24. Ojha, L., Buffo, J. & Journaux, B. Thermophysical arguments against basal melting in the south polar region of Mars. *Icarus* **407**, 115772 (2024).
25. Clifford, S. M. et al. Depth of the Martian cryosphere: revised estimates and implications for the existence and detection of subpermafrost groundwater. *J. Geophys. Res.* **115**, 2009JE003462 (2010).
26. Li, C. et al. Layered subsurface in Utopia Basin of Mars revealed by Zhurong rover radar. *Nature* **610**, 308–312 (2022).
27. Bormann, P., Engdahl, E. R. & Kind, R. Seismic wave propagation and earth models. *New Manual of Seismological Observatory Practice 2 (NMSOP2)* 8 mb, 105 https://doi.org/10.2312/GFZ.NMSOP-2_CH2 (2012).
28. Lognonné, P. et al. SEIS: insight's seismic experiment for internal structure of Mars. *Space Sci. Rev.* **215**, 12 (2019).
29. Manga, M. & Wright, V. No cryosphere-confined aquifer below InSight on Mars. *Geophys. Res. Lett.* **48**, e2021GL093127 (2021).
30. Wright, V., Morzfeld, M. & Manga, M. Liquid water in the Martian mid-crust. *Proc. Natl. Acad. Sci. USA* **121**, e2409983121 (2024).
31. Menina, S. et al. Energy envelope and attenuation characteristics of high-frequency (HF) and Very-High-Frequency (VF) Martian Events. *Bull. Seismol. Soc. Am.* **111**, 3016–3034 (2021).
32. Lognonné, P. et al. Constraints on the shallow elastic and anelastic structure of Mars from InSight seismic data. *Nat. Geosci.* **13**, 213–220 (2020).
33. Saar, M. O. & Manga, M. Seismicity induced by seasonal groundwater recharge at Mt. Hood, Oregon. *Earth Planet. Sci. Lett.* **214**, 605–618 (2003).
34. Christiansen, L., Hurwitz, S., Saar, M., Ingebritsen, S. & Hsieh, P. Seasonal seismicity at western United States volcanic centers. *Earth Planet. Sci. Lett.* **240**, 307–321 (2005).
35. Ekström, G., Nettles, M. & Tsai, V. C. Seasonality and increasing frequency of greenland glacial earthquakes. *Science* **311**, 1756–1758 (2006).
36. Bao, X. & Eaton, D. W. Fault activation by hydraulic fracturing in western Canada. *Science* **354**, 1406–1409 (2016).
37. InSight Marsquake Service. Mars Seismic Catalogue, InSight Mission; V14 2023-04-01. *ETHZ, IPGP, JPL, ICL, Univ. Bristol*. https://doi.org/10.12686/a21 (2023).
38. Clinton, J. F. et al. The Marsquake catalogue from InSight, sols 0–478. *Phys. Earth Planet. Inter.* **310**, 106595 (2021).
39. Van Driel, M. et al. High-frequency seismic events on Mars observed by insight. *JGR Planets* **126**, e2020JE006670 (2021).
40. Knapmeyer, M. et al. Seasonal seismic activity on Mars. *Earth Planet. Sci. Lett.* **576**, 117171 (2021).
41. Ceylan, S. et al. The Marsquake catalogue from InSight, sols 0–1011. *Phys. Earth Planet. Inter.* **333**, 106943 (2022).
42. Senapati, B., Kundu, B., Jha, B. & Jin, S. Gravity-induced seismicity modulation on planetary bodies and their natural satellites. *Sci. Rep.* **14**, 2311 (2024).
43. Gutenberg, B. & Richter, C. F. Frequency of earthquakes in California. *Bull. Seismol. Soc. Am.* **34**, 185–188 (1944).
44. Zhang, L., Zhang, J., Mitchell, R. N., Cao, P. & Liu, J. A thermal origin for super-high-frequency marsquakes. *Icarus* **390**, 115327 (2023).
45. Moore, P. L. et al. Glacier slip and seismicity induced by surface melt. *Geology* **41**, 1247–1250 (2013).
46. Lognonné, P. et al. Mars seismology. *Annu. Rev. Earth Planet. Sci.* **51**, 643–670 (2023).
47. Lammlein, D. R. Lunar seismicity and tectonics. *Phys. Earth Planet. Inter.* **14**, 224–273 (1977).
48. Ruíz, M. et al. Meteorological changes across Curiosity rover's Traverse using REMS measurements and comparisons between measurements and MRAMS model results. *Remote Sens.* **17**, 368 (2025).
49. Keranen, K. M., Weingarten, M., Abers, G. A., Bekins, B. A. & Ge, S. Sharp increase in central Oklahoma seismicity since 2008 induced by massive wastewater injection. *Science* **345**, 448–451 (2014).
50. Stein, R. S. The role of stress transfer in earthquake occurrence. *Nature* **402**, 605–609 (1999).
51. Dahmen, N. L. et al. Super high frequency events: a new class of events recorded by the inSight seismometers on Mars. *JGR Planets* **126**, e2020JE006599 (2021).
52. Clinton, J. et al. The Marsquake service reference catalogue. in EGU25-13152 https://doi.org/10.5194/egusphere-egu25-13152 (2025).
53. Ikari, M. J., Saffer, D. M. & Marone, C. Effect of hydration state on the frictional properties of montmorillonite-based fault gouge. *J. Geophys. Res.* **112**, 2006JB004748 (2007).
54. Cornelio, C., Spagnuolo, E., Di Toro, G., Nielsen, S. & Violay, M. Mechanical behaviour of fluid-lubricated faults. *Nat. Commun.* **10**, 1274 (2019).
55. Stähler, S. C. et al. Tectonics of Cerberus Fossae unveiled by Marsquakes. *Nat. Astron* **6**, 1376–1386 (2022).
56. Onodera, K., Kawamura, T., Tanaka, S., Ishihara, Y. & Maeda, T. Numerical simulation of lunar seismic wave propagation: investigation of subsurface scattering properties near Apollo 12 landing site. *J. Geophys. Res. Planets* **126**, e2020JE006406 (2021).
57. Gillet, K., Margerin, L., Calvet, M. & Monnereau, M. Scattering attenuation profile of the Moon: implications for shallow moonquakes and the structure of the megaregolith. *Phys. Earth Planet. Inter.* **262**, 28–40 (2017).
58. Zenhäusern, G. et al. An estimate of the impact rate on Mars from statistics of very-high-frequency marsquakes. *Nat. Astron* **8**, 1138–1147 (2024).

59. Scholz, C. H. On the stress dependence of the earthquake *b* value. *Geophys. Res. Lett.* **42**, 1399–1402 (2015).
60. Schorlemmer, D., Wiemer, S. & Wyss, M. Variations in earthquake-size distribution across different stress regimes. *Nature* **437**, 539–542 (2005).
61. Scholz, C. H. The frequency-magnitude relation of microfracturing in rock and its relation to earthquakes. *Bull. Seismol. Soc. Am.* **58**, 399–415 (1968).
62. Bachmann, C. E., Wiemer, S., Goertz-Allmann, B. P. & Woessner, J. Influence of pore-pressure on the event-size distribution of induced earthquakes. *Geophys. Res. Lett.* **39**, 2012GL051480 (2012).
63. Knapmeyer, M. et al. The global seismic moment rate of Mars after event S1222a. *Geophys. Res. Lett.* **50**, e2022GL102296 (2023).
64. Wiemer, S. & McNutt, S. Variations in the frequency-magnitude distribution with depth in two volcanic areas: Mount St. Helens, Washington, and Mt. Spurr, Alaska. *Geophys. Res. Lett.* **24**, 189–192 (1997).
65. Podolskiy, E. A. & Walter, F. Cryoseismology. *Rev. Geophys.* **54**, 708–758 (2016).
66. Millour, E. et al. The Mars Climate Database (Version 6.1). https://meetingorganizer.copernicus.org/EPSC2022/EPSC2022-786.html, https://doi.org/10.5194/epsc2022-786 (2022).
67. Grott, M. et al. Thermal conductivity of the martian soil at the InSight landing site from HP^3 active heating experiments. *JGR Planets* **126**, e2021JE006861 (2021).
68. Hartlieb, P., Toifl, M., Kuchar, F., Meisels, R. & Antretter, T. Thermo-physical properties of selected hard rocks and their relation to microwave-assisted comminution. *Miner. Eng.* **91**, 34–41 (2016).
69. Li, D. et al. Phase diagrams and thermochemical modeling of salt lake brine systems. II. NaCl+H2O, KCl+H2O, MgCl2+H2O and CaCl2+H2O systems. *Calphad* **53**, 78–89 (2016).
70. Wang, Y. et al. Permafrost thawing under overlaying salt water. *Sci. Adv.* **11**, eadp2808 (2025).
71. Peña Castro, A. F. et al. Stress chatter via fluid flow and fault slip in a hydraulic fracturing-induced earthquake sequence in the Montney formation, British Columbia. *Geophys. Res. Lett.* **47**, e2020GL087254 (2020).
72. Manga, M., Zhai, G. & Wang, C. Squeezing Marsquakes out of groundwater. *Geophys. Res. Lett.* **46**, 6333–6340 (2019).
73. Morgan, G. A. et al. Refined mapping of subsurface water ice on Mars to support future missions. *Planet. Sci. J.* **6**, 29 (2025).
74. Posiolova, L. V. et al. Largest recent impact craters on Mars: orbital imaging and surface seismic co-investigation. *Science* **378**, 412–417 (2022).
75. Liu, Y. et al. Zhurong reveals recent aqueous activities in Utopia Planitia, Mars. *Sci. Adv.* **8**, eabn8555 (2022).
76. Hou, Z. et al. The search for life signatures on Mars by the Tianwen-3 Mars sample return mission. *Natl. Sci. Rev.* **11**, nwae313 (2024).
77. Muirhead, B. K., Nicholas, A. K., Umland, J., Sutherland, O. & Vijendran, S. Mars sample return campaign concept status. *Acta Astron.* **176**, 131–138 (2020).
78. Roth, N., Zhu, T. & Gao, Y. Characterizing liquid water in deep martian aquifers: a seismo-electric approach. *JGR Planets* **129**, e2024JE008292 (2024).
79. Deng, K., Liu, Y. & Harrington, R. M. Poroelastic stress triggering of the December 2013 Crooked Lake, Alberta, induced seismicity sequence. *Geophys. Res. Lett.* **43**, 8482–8491 (2016).
80. McGarr, A. Maximum magnitude earthquakes induced by fluid injection: limits on fluid injection earthquakes. *J. Geophys. Res. Solid Earth* **119**, 1008–1019 (2014).
81. Kawamura, T. et al. S1222a—the largest marsquake detected by InSight. *Geophys. Res. Lett.* **50**, e2022GL101543 (2023).
82. Hamid, S. S., Kerber, L., Clarke, A. B. & Forget, F. The delivery of water ice to the Martian surface by passive degassing. *Icarus* **416**, 116084 (2024).
83. Qin, X. et al. Modern water at low latitudes on Mars: potential evidence from dune surfaces. *Sci. Adv.* **9**, eadd8868 (2023).
84. Clark, B. C. & Van Hart, D. C. The salts of Mars. *Icarus* **45**, 370–378 (1981).
85. Toner, J. D., Catling, D. C. & Light, B. Ton. *Icarus* **250**, 451–461 (2015).
86. Shillington, D. J. et al. Link between plate fabric, hydration and subduction zone seismicity in Alaska. *Nat. Geosci.* **8**, 961–964 (2015).
87. Utsu, T. Representation and analysis of the earthquake size distribution: a historical review and some new approaches. *Pure Appl. Geophys.* **155**, 509–535 (1999).
88. Roberts, N. S., Bell, A. F. & Main, I. G. Are volcanic seismic b-values high, and if so when? *J. Volcanol. Geotherm. Res.* **308**, 127–141 (2015).
89. Qi, C. et al. Crystallographic preferred orientations of ice deformed in direct-shear experiments at low temperatures. *Cryosphere* **13**, 351–371 (2019).
90. Hanks, T. C. & Kanamori, H. A moment magnitude scale. *J. Geophys. Res.* **84**, 2348–2350 (1979).
91. Ben-Zion, Y. Collective behavior of earthquakes and faults: continuum-discrete transitions, progressive evolutionary changes, and different dynamic regimes. *Rev. Geophys.* **46**, 2008RG000260 (2008).
92. Schultz, R. A. Limits on strength and deformation properties of jointed basaltic rock masses. *Rock. Mech. Rock. Eng.* **28**, 1–15 (1995).
93. Chang, X., Liu, W., Zuo, G., Dou, Y. & Li, Y. Research on ultrasonic-based investigation of mechanical properties of ice. *Acta Oceanol. Sin.* **40**, 97–105 (2021).
94. Forget, F. Improved optical properties of the Martian atmospheric dust for radiative transfer calculations in the infrared. *Geophys. Res. Lett.* **25**, 1105–1108 (1998).
95. Madeleine, J.-B., Forget, F., Millour, E., Montabone, L. & Wolff, M. J. Revisiting the radiative impact of dust on Mars using the LMD Global Climate Model. *J. Geophys. Res.* **116**, E11010 (2011).
96. Montabone, L. et al. Eight-year climatology of dust optical depth on Mars. *Icarus* **251**, 65–95 (2015).
97. Shi, J. & Li, J. Near-surface liquid water on Mars inferred from seasonal Marsquakes. Zenodo https://doi.org/10.5281/zenodo.17765768 (2025).
98. Daubar, I. J. et al. New craters on Mars: an updated catalog. *JGR Planets* **127**, e2021JE007145 (2022).

Acknowledgements

J.L. acknowledges funding from National Key R&D Program of China (2022YFF0503203, 2024YFF0809900) and National Natural Science Foundation of China (42441827, 42474226). J.S. is supported by the China Postdoctoral Science Foundation under Grant Number 2025M780362. S.F. and C.S. acknowledge funding from the National Natural Science Foundation through grant No. 42475133. H.M. acknowledge funding from the National Natural Science Foundation through grant No. 42474083. H.M., C.S., and S.F. acknowledge the High Level Special Fund of Southern University of Science and Technology (Grant No. G03050K001). T.W. is funded by the Fundamental Research Funds for the Central Universities (Grant 2023300298). We acknowledge NASA, CNES, their partner agencies and institutions (UKSA, SSO, DLR, JPL, IPGP-CNRS, ETHZ, IC, MPS-MPG), and the flight operations team at JPL, SISMOC, MSDS, IRIS-DMC, and PDS for providing SEED SEIS data. We are grateful to the Marsquake Service Team to provide the marsquake catalogue. J.L. thanks Chi-Yuen Wang, Hongyu Yu, Bei Wang, Ke Xu, Xing Wu, and Michael Manga for valuable discussions.

Author contributions

J.L. designed the project. J.S. and J.L. conducted the main investigation. J.S. produced all figures. C.L. and C.Q. carried out the laboratory experiments on brine percolation. H.M. provided depth profiles of heat conduction and estimates of fault slip length. C.S. and S.F. calculated the surface temperatures of Mars. Z.T. analyzed the stress variations induced by the Sun and Phobos. L.P. analyzed the geological environment of Mars. T.W., L.X., X.H., and L.C. provided estimates of pore pressure. J.S. and J.L. drafted the manuscript. All authors contributed to data interpretation, discussion, and revision of the manuscript.

Competing interests

The authors declare no competing interests.

Additional information

Supplementary information The online version contains supplementary material available at https://doi.org/10.1038/s41467-025-67784-4.

Correspondence and requests for materials should be addressed to Jiaqi Li.

Peer review information *Nature Communications* thanks Lujendra Ojha and Tieyuan Zhu for their contribution to the peer review of this work. A peer review file is available.

Reprints and permissions information is available at http://www.nature.com/reprints

---

[1]SKLab-DeepMinE, MOEKLab-OBCE, School of Earth and Space Sciences, Peking University, Beijing, China. [2]Research Institute of Extraterrestrial Material, Peking University, Beijing, China. [3]NWU-HKU Joint Center of Earth and Planetary Sciences, Department of Geology, Northwest University, Xi'an, China. [4]Key Laboratory of Earth and Planetary Physics, Institute of Geology and Geophysics, Chinese Academy of Sciences, Beijing, China. [5]College of Earth and Planetary Sciences, University of Chinese Academy of Sciences, Beijing, China. [6]Department of Earth and Space Sciences, Southern University of Science and Technology, Shenzhen, China. [7]Center for High Pressure Science and Technology Advanced Research, Beijing, China. [8]National Key Laboratory of Deep Space Exploration/School of Earth and Space Sciences, University of Science and Technology of China, Hefei, China. [9]Frontiers Science Center for Critical Earth Material Cycling, School of Earth Sciences and Engineering, Nanjing University, Nanjing, China. [10]College of Urban and Environmental Sciences, Peking University, Beijing, China. [11]State Key Laboratory of Lithospheric and Environmental Coevolution, Institute of Geology and Geophysics, Chinese Academy of Sciences, Beijing, China. ✉e-mail: JLI@pku.edu.cn